Nano Research

ISSN 1998-0124 CN 11-5974/O4
https://doi.org/10.1007/s12274-022-4179-8

Research Article

Non-noble metal-based amorphous high-entropy oxides as efficient and reliable electrocatalysts for oxygen evolution reaction

Qianqian Wang[1,2], Jiaqi Li[1], Yongjie Li[1], Genmiao Shao[1], Zhe Jia[1], and Baolong Shen[1] (✉)

[1] *School of Materials Science and Engineering, Jiangsu Key Laboratory for Advanced Metallic Materials, Southeast University, Nanjing 211189, China*
[2] *School of Materials Science and Engineering, Jiangsu Key Laboratory of Advanced Structural Materials and Application Technology, Nanjing Institute of Technology, Nanjing 211167, China*

Received: 28 November 2021 / **Revised:** 9 January 2022 / **Accepted:** 19 January 2022

ABSTRACT

Exploring high-performance and cost-effective electrocatalysts that are applicable in oxygen evolution reaction (OER) is crucial for water splitting and energy storage. In this work, a facile and scalable chemical reduction strategy is developed to synthesize FeCoNiPB non-noble metal-based amorphous high-entropy oxides for the OER in alkaline media. The FeCoNiPB oxides exhibit overpotentials of 235 and 306 mV at current densities of 10 and 100 mA/cm^2, respectively, as well as a small Tafel slope of 53 mV/dec in 1.0 M KOH solution, outperforming the performance of FeCoPB, FeNiPB, and CoNiPB oxides and the commercial RuO_2, while maintaining excellent stability with negligible overpotential amplification over 40 h. The superior OER electrocatalytic efficiency and stability of the FeCoNiPB catalyst is primarily attributed to its unique amorphous high-entropy nanostructure, synergistic effect of the multiple components, and *in situ*-formed amorphous sheets with a thin (FeCoNi)OOH crystalline layer on the edge during long-term OER. This work provides new insights to design and prepare low-cost, highly efficient, and durable OER electrocatalysts.

KEYWORDS

FeCoNiPB, amorphous high-entropy oxides, oxygen evolution reaction, synergistic effect, self-reconstruction

1 Introduction

Due to the increasing demands of traditional fossil fuels and the ecological environment destruction induced by their overconsumption, exploring eco-friendly, reproducible, and highly efficient energy sources such as hydrogen has attracted substantial attention over the past decades [1, 2]. Among various feasible methods to produce hydrogen, electrochemical water splitting has been identified as a particularly promising and appealing technology, which opens up the possibility of replacing traditional fossil fuels with a carbon neutral alternative [3, 4]. The whole water splitting system comprises two significant half-reactions, which are termed the hydrogen evolution reaction (HER) and oxygen evolution reaction (OER) occurring in the cathode and anode of an electrolyzer, respectively. Due to the sluggish kinetics caused by the multiple proton coupled electron transfer (PCET) process, the OER has severely impeded the efficiency of water splitting and the rate of hydrogen generation [5]. In addition, the OER also plays a significant role in energy storage and conversion technologies, especially in rechargeable metal-air batteries and renewable fuel cells [6, 7]. While the commercial OER catalysts, such as IrO_2 and RuO_2, exhibit high OER catalytic activity, their high cost, poor scalability, and scarcity are the major impediments [8]. Accordingly, there is a great demand for the scalable synthesis of cost-effective, high-performance, and stable electrocatalysts to substitute for currently used high-cost materials.

Designing complex alloys with dissimilar metals has shown advantages in enhancing their catalytic activity [9–11]. The alloying of multiple metals can increase disordered configurational entropy to generate more active sites and supply optimum surface absorption energy for catalysis [12–14]. Specifically, high-entropy alloys (HEAs) with five or more elements alloying into a single phase solid solution, which originally attracted great attention because of their high performance in mechanical properties [15], have been reported to be advantageous in catalytic performance recently [16–18]. Basically, HEAs not only have high catalytic activity due to the severe lattice distortion effect and tunable d-band center, but also show superb stability owing to their high entropy effect [19, 20]. In addition, compared with crystalline materials, amorphous materials with a large number of insufficiently coordinated atoms and structural defects provide more reaction sites, which is beneficial to improve the catalytic performance [21–28]. Thus, amorphous high-entropy materials may have promising catalytic performance for chemical reactions [29].

Transition metals, including iron (Fe), cobalt (Co), and nickel (Ni), with low material cost and tunable electronic structure are well studied in OER catalysis [30–32]. Especially, the NiFe (oxy)hydroxides are considered as the benchmark electrocatalysts for OER in alkaline solution [33, 34]. However, the amorphous-forming ability (AFA) of these transition metals is poor. To obtain amorphous structures, metalloids such as P, B, Si, and C are usually introduced in the transition metal-based alloys to stabilize the long-range disordered structure [35]. Besides, designing transition metal-metalloid compounds is generally believed to be a

Address correspondence to blshen@seu.edu.cn

valid strategy to improve the intrinsic activity of electrocatalysts via the synergistic effect [36–38]. The charge transfer between different elements can modulate the electronic configuration to reduce the kinetic energy barriers during the electrochemical reaction [39, 40]. It was reported that electrons can move from Ni, Fe, or Co to P in transition metal phosphides, thus P atoms become negatively charged and serve as active catalytic centers [41, 42]. Conversely, transition metal borides possess superior OER catalytic properties via opposite electron transfer paths, i.e., electrons transfer from B to Ni, Fe, or Co [42, 43]. As a result, alloying of P and B may introduce synergistic effect for not only AFA but also catalytic processes.

Recently, several methods have been developed to synthesize HEA and amorphous high-entropy nanoparticles. For example, the laser synthesis and processing of colloids (LSPC) is a straightforward, scalable, and surfactant-free solution, and HEA and amorphous high-entropy nanoparticles with diameter between 5–22 nm have been synthesized and exhibited excellent electrochemical catalytic performance [29, 44, 45]. And the chemical reduction method is a facile method and can introduce O element in the alloy to facilitate the catalytic performance [46]. In this work, we employ a chemical reduction approach to prepare FeCoNiPB non-noble metal-based amorphous high-entropy oxides, enabling fine tuning of the electronic structure to improve the OER catalytic performance. To highlight the superiority of the high-entropy effect, the OER catalytic performance is compared with that of binary metal-based counterparts, including FeCoPB, FeNiPB, and CoNiPB oxides. The overpotential and Tafel slope of FeCoNiPB catalyst are much smaller than those of binary metal-based nanomaterials, as the amorphous high-entropy nanostructure provides abundant highly efficient active sites that contribute to OER activity. Furthermore, a self-reconstructed amorphous sheet with a thin (FeCoNi)OOH crystalline layer on the edge formed during long-term chronopotentiometry tests gives rise to an increased number of active sites that maintain excellent stability. The design strategy of non-noble metal-based amorphous high-entropy oxides may stimulate the discovery of high-performance electrocatalytic materials that can be produced at the industrial scale.

2 Experimental section

2.1 Materials synthesis

FeCoNiPB samples were synthesized by a facile and scalable chemical reduction method. Primarily, 0.003 mol of metal salts ($FeCl_2{\cdot}4H_2O$, $CoCl_2{\cdot}6H_2O$, and $NiCl_2{\cdot}6H_2O$) and 0.012 mol of sodium hypophosphite ($NaH_2PO_2{\cdot}H_2O$) were dissolved in 50 mL of deionized water. Meanwhile, 15 mL of sodium borohydride ($NaBH_4$, 0.006 mol) fresh aqueous solution was added dropwise into the abovementioned solution at a rate of 5 mL/min using a constant-flow pump. The reaction process was executed for 50 min under high-purity nitrogen protection and mechanical stirring at room temperature. Then the resultant precipitates were collected by extraction filtration after washing with deionized water and ethanol in sequence for three times. The samples were then dried in vacuum at room temperature overnight. The FeCoPB, FeNiPB, and CoNiPB samples were prepared using the same procedure as that of FeCoNiPB, without adding nickel salt ($NiCl_2{\cdot}6H_2O$), cobalt salt ($CoCl_2{\cdot}6H_2O$), or iron salt ($FeCl_2{\cdot}4H_2O$).

2.2 Materials characterizations

The morphology and microstructure of the samples were characterized by scanning electron microscopy (SEM, Zeiss Supra55) and transmission electron microscopy (TEM, Tecnai G2 F3). The composition of the samples was analyzed using energy dispersive spectroscopy (EDS) equipped in the TEM. The phase of the catalysts was analyzed by X-ray diffraction (XRD, D8-Discover) using Cu Kα radiation (λ = 1.54 Å). X-ray photoelectron spectroscopy (XPS, Thermo Fisher Nexsa) with an Al Kα (1,486.6 eV) X-ray source was used to investigate the binding energies of the elements on the surface. The calibration was carried out using C 1s (284.80 eV) as charge compensation. The samples for XPS analyses were preserved in vacuum before tests. The specific surface area and pore size distribution were analyzed by N_2 absorption and desorption isotherms with a Brunauer–Emmett–Teller (BET) method (QuadraSorb Station 1). Prior to the N_2 adsorption experiment, the catalyst powders were degassed at 423 K for 2 h.

2.3 Electrochemical measurements

All electrochemical tests were conducted in a standard three-electrode cell configuration using an electrochemical workstation (Gamary Interface 1000) at room temperature. A Pt sheet and a standard Hg/HgO electrode were used as the counter electrode and the reference electrode, respectively. The Hg/HgO electrode was calibrated using potassium ferricyanide solution before initial use, with details shown in Fig. S1 in the Electronic Supplementary Material (ESM) [47]. For the working electrode, catalyst inks were prepared by dispersing catalyst powder (5 mg) in a mixture of deionized water (500 μL), ethanol (480 μL), and 5% nafion (20 μL) and ultrasonicated for 1 h. Subsequently, 3 μL of ink was uniformly drop-cast onto a polished glassy carbon electrode (GCE) (0.0707 cm^2) to obtain a loading density of 0.2 mg/cm^2, and then dried in air.

1.0 M KOH was used as the electrolyte for OER measurements. The potential data were converted to the potential vs. reversible hydrogen electrode (RHE) according to equation (E(RHE) = E(Hg/HgO) + 0.0591 × pH + 0.098 V). The overpotential (η) was calculated as follows $\eta = E$ vs. RHE 1.23 V. In addition, all polarization current densities were normalized to the geometric surface area. Linear sweep voltammetry (LSV) measurements for the OER were performed at a scan rate of 5 mV/s. The Tafel slope was determined by the linear region of the LSV polarization curves which can be fitted using the Tafel equation ($\eta = b \times \log j + a$, where b represents the Tafel slope and j denotes the current density). Electrochemical impedance spectroscopy (EIS) was recorded at an overpotential of 300 mV in a frequency range from 10 kHz to 0.1 Hz. The chronopotentiometry test (constant current density = 10 mA/cm^2) was employed to investigate the long-term stability of the electrocatalyst on carbon fiber paper (CFP) at a loading density of 0.7 mg/cm^2. The double-layer capacitance (C_{dl}) of the electrocatalysts was estimated through cyclic voltammetry at different scan rates of 10, 20, 30, 40, and 50 mV/s in the non-Faradic potential region. The C_{dl} value was obtained by plotting $\Delta j = (j_a - j_c)$ at 1.09 V (vs. RHE) corresponding to the scan rates, and the fitting slope of the linear line was twice the value of C_{dl}. The electrochemically active surface area (ECSA) was measured from the double-layer capacitance according to the following equation ECSA = C_{dl}/C_s, where C_s is the specific capacitance value of 0.040 mF/cm^2 in a 1.0 M KOH solution [48].

3 Results and discussion

Figure 1(a) presents a schematic illustration of the synthetic process of FeCoNiPB non-noble metal-based amorphous high-entropy oxides via the facile chemical reduction method. The unique self-reconstructed amorphous sheets with a thin (FeCoNi)OOH crystalline layer on the edge are *in-situ* evolved during the long-term OER test, which will be revealed in a later

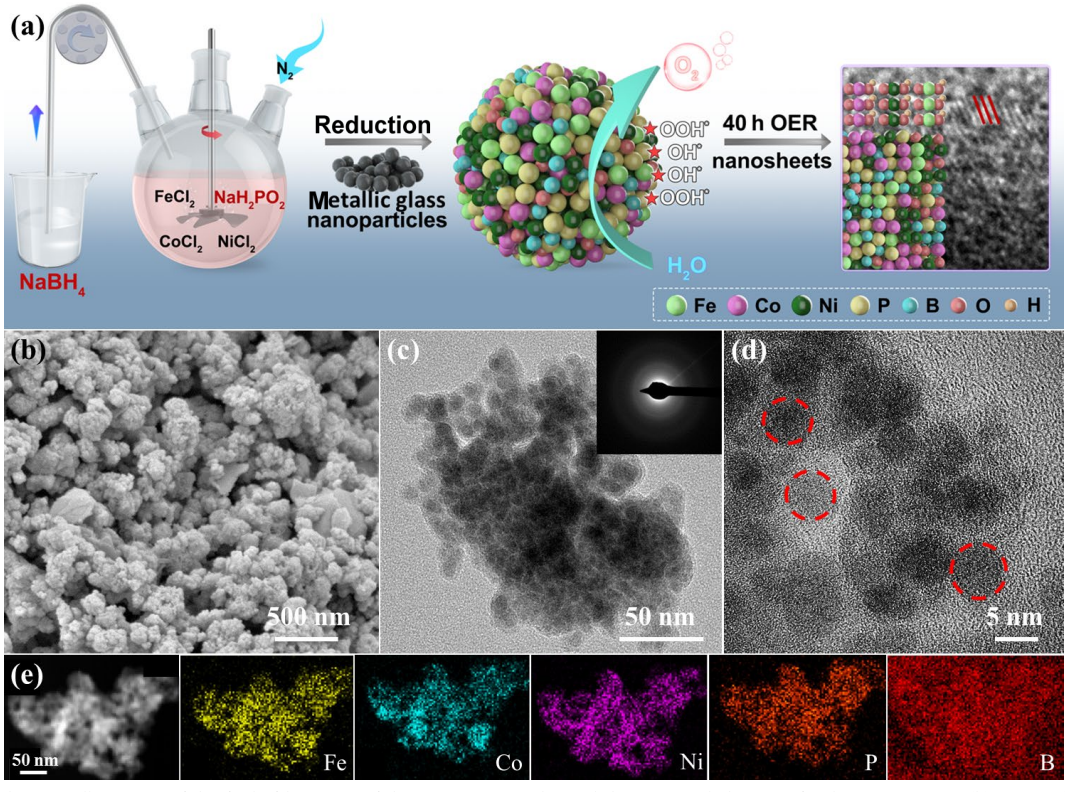

Figure 1 (a) Schematic illustration of the facile fabrication of the FeCoNiPB oxides and the structural changes after long-term OER. (b) SEM, (c) TEM, and (d) HRTEM images of the as-prepared FeCoNiPB sample. The inset of (c) shows the corresponding SAED pattern. (e) HAADF image and elemental mappings of the as-prepared FeCoNiPB sample.

section. The morphologies of the as-prepared FeCoPB, FeNiPB, and CoNiPB samples were analyzed using SEM, and the images are shown in Figs. S2(a), S2(c), and S2(e) in the ESM. It was found that the FeCoPB sample exhibits flower-like nanosheets structure; the FeNiPB presents a structure of nanoparticles wrapped by fibers, and the CoNiPB is composed of nanoparticles. The SEM image of the as-prepared FeCoNiPB sample is shown in Fig. 1(b). With the simultaneous existence of Fe, Co, and Ni elements, the FeCoNiPB sample shows nanoparticles together with some random appearance of nanosheets. It seems that the nanosheet/nanofiber-like structure only exists in the samples that contain Fe. The varied morphologies of the samples affect their exposed surface areas, which is an important parameter for electrochemical catalysis. The specific surface areas of the samples were obtained via the BET method, and the N_2 adsorption–desorption isotherm curves and pore size distribution curves of the samples are shown in Fig. S3 in the ESM. The specific surface areas of the FeCoPB, FeNiPB, CoNiPB, and FeCoNiPB samples are 238.1, 138.3, 19.2, and 45.6 m^2/g, respectively. The FeCoPB sample has the largest BET surface area, while the CoNiPB sample shows the smallest surface area. The difference in the specific surface areas of the samples is related to their morphologies, as the nanosheets have a higher exposed surface area than the nanoparticles.

The nanostructure of the as-prepared samples was analyzed by TEM, with the image of the FeCoNiPB sample shown in Fig. 1(c), and the images of the FeCoPB, FeNiPB, and CoNiPB samples are shown in Figs. S2(b), S2(d), and S2(f) in the ESM. The TEM morphologies of the four samples are consistent with those obtained from SEM. Nevertheless, it is noteworthy that the CoNiPB nanoparticles show a wider size distribution, while the size of the FeCoNiPB nanoparticles is more identical. The selected area electron diffraction (SAED) patterns of the four samples are shown in the insets of corresponding images. The SAED patterns of both the FeCoPB and FeNiPB samples show multiple diffraction rings, indicating the existence of multiple phases and the samples are partially crystallized. The SAED patterns of CoNiPB and FeCoNiPB samples only exhibit one large halo, confirming the amorphous nature of these two samples. With a closer observation of the FeCoNiPB nanoparticles using high-resolution TEM (HRTEM), as shown in Fig. 1(d), spherical nanoparticles with an average size of 5–10 nm are observed. The nanoparticles are agglomerated owing to the high surface energy. No lattice plane from crystalline phases is observed, further corroborating the amorphous structure of the FeCoNiPB nanoparticles. Figure 1(e) shows the high-angle annular dark field (HAADF) image of the FeCoNiPB nanoparticles and the EDS elemental mappings of the Fe, Co, Ni, P, and B, revealing the homogeneous distribution of the constituents. The elemental mapping result of O is also homogeneously distributed, as shown in Fig. S4 in the ESM. The elemental mappings of the FeCoPB, FeNiPB, and CoNiPB samples were also analyzed, showing an even distribution of the composed elements and O, as shown in Figs. S5–S7 in the ESM. Hence, these results indicate that the strong reducing agent $NaBH_4$ and weak reducing agent NaH_2PO_2 release a large amount of B and P atoms during the reduction process, which are simultaneously doped into the metal matrix, realizing the stabilization of the amorphous structure. The compositions of the as-prepared FeCoPB, FeNiPB, CoNiPB, and FeCoNiPB catalysts measured by EDS are listed in Table S1 in the ESM. All of the samples contain a high concentration of O, and the FeCoNiPB has the highest amount of O. Other than O, relatively significant differences of the metals and metalloids are found in FeCoPB, FeNiPB, and CoNiPB samples, but not in FeCoNiPB sample. The quasi-equimolar composition of FeCoNiPB may due to the competition among the three transition metals during the chemical reduction of preparation process.

Phase characterization of the as-prepared FeCoNiPB, FeCoPB, FeNiPB, and CoNiPB samples was carried out using XRD, as shown in Fig. 2(a). All patterns have a broad diffraction peak

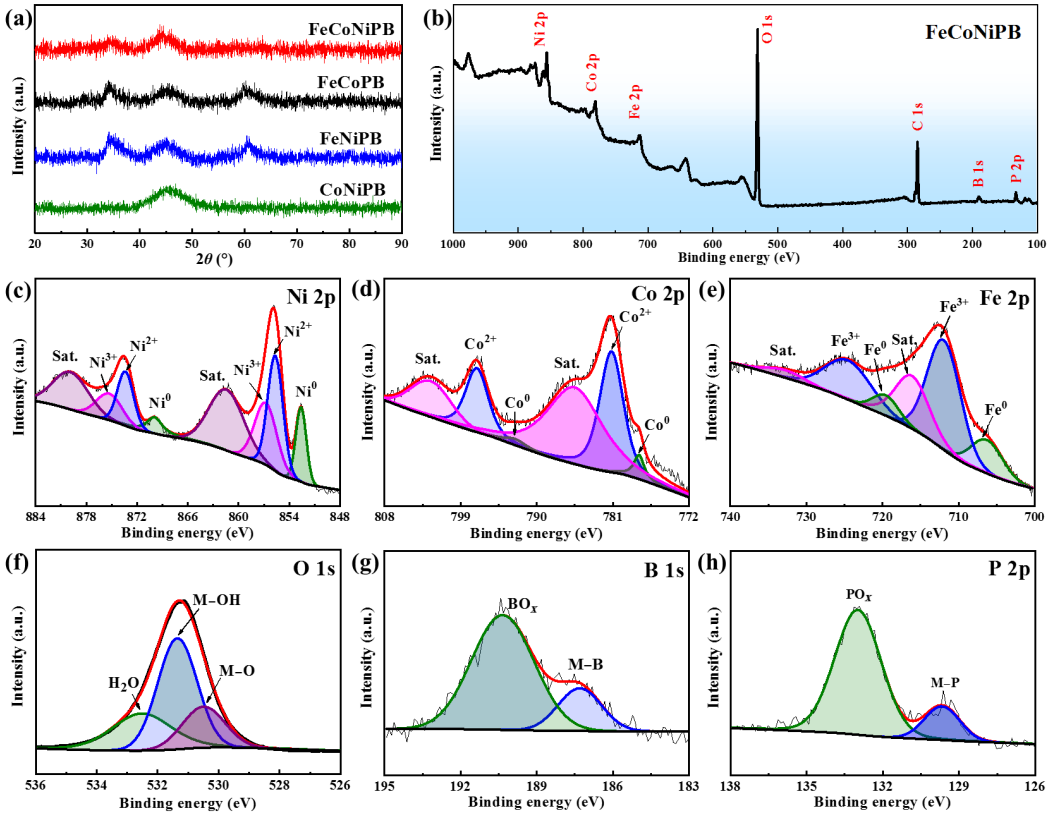

Figure 2 (a) XRD patterns of the as-prepared samples. XPS analyses of the as-prepared FeCoNiPB oxides: (b) full spectrum, (c) Ni 2p, (d) Co 2p, (e) Fe 2p, (f) O 1s, (g) B 1s, and (h) P 2p.

around $2\theta \approx 45°$, confirming their amorphous structures. In addition, FeCoPB and FeNiPB exhibit two shoulder peaks at $2\theta \approx 35°$ and 61°, deriving from the formation of metal oxides during preparation and measurements under atmospheric exposure [49]. This is consistent with their SAED results.

The surface chemistry and electronic structure of the as-prepared samples were investigated by XPS. The full spectrum and high-resolution XPS spectra of Ni 2p, Co 2p, Fe 2p, O 1s, B 1s, and P 2p for FeCoNiPB catalyst are shown in Figs. 2(b)–2(h), while the XPS spectra for FeCoPB, FeNiPB, and CoNiPB samples are shown in Figs. S8–S10 in the ESM. The corresponding binding energies are summarized in Table S2 in the ESM. The full XPS spectrum in Fig. 2(b) confirms the existence of Fe, Co, Ni, P, B, and O in the FeCoNiPB catalyst. For the Ni 2p spectrum in Fig. 2(c), the binding energy of 852.6 eV ($2p_{3/2}$) corresponds to the interaction of metallic Ni^0 with metalloids in FeCoNiPB [40]. The peaks of oxidized species ($Ni^{2+/3+}$) are ascribed to exposure to the atmosphere and water during preparation. The content of Ni^0 in FeCoNiPB is higher than that in FeNiPB but lower than that in CoNiPB. The Co 2p spectrum in Fig. 2(d) shows two major peaks at 777.8 eV ($2p_{3/2}$) and 781.1 eV ($2p_{3/2}$), which are attributed to Co^0 and Co^{2+} [50]. Due to the oxidation in FeCoPB, the Co 2p spectrum shows only the oxidized species $Co^{2+/3+}$, without the appearance of Co^0. In contrast, the Co element in CoNiPB only shows the peaks of Co^0 and Co^{2+}. As shown in Fig. 2(e), the Fe $2p_{3/2}$ in FeCoNiPB shows two main peaks at 706.3 eV ($2p_{3/2}$) and 711.9 eV ($2p_{3/2}$), which are attributed to Fe^0 and Fe^{3+}, respectively [19]. Nevertheless, the peak of Fe^0 in FeNiPB is weaker than that in FeCoNiPB, and FeCoPB is entirely oxidized to $Fe^{2+/3+}$, resulting in the absence of the Fe^0 peak. Based on the binding energy analysis of transition metals, FeCoNiPB maintains both the zero valence and oxidation states of transition metals, displaying a moderate degree of oxidation compared to those of binary transition metal-based counterparts. According to the O 1s spectra for the FeCoNiPB, FeNiPB, CoNiPB, and FeCoPB samples, three main peaks attributed to the oxygen in metal oxides, hydroxyl groups and surface-absorbed water molecules, can be detected in all four samples [40]. The peak area calculation from EDS further confirms the high degree of oxidation in the catalysts, i.e., FeCoPB (78.4%), FeNiPB (75.3%), FeCoNiPB (71.8%), and CoNiPB (70.9%). The high oxidation degree of the four samples provides a large amount of active sites on the surface to facilitate OER reaction [49].

In addition to the chemical states of metallic elements, the binding energies of metalloids B and P in the nanoparticles also have significant impacts on the catalytic properties. The B 1s spectrum in Fig. 2(g) displays two peaks at 187.3 and 190.3 eV, corresponding to the zero-valent B in metal boride and the oxidized B, respectively [43]. Similarly, the P 2p spectrum in Fig. 2(h) reveals two peaks at 129.7 and 133.0 eV, derived from zero-valent phosphorus in metal phosphide and phosphate [51]. Compared with pure B (187.0 eV) and P (130.2 eV) [52], the peaks of zero-valent B and P in FeCoNiPB exhibit positive and negative shifts, respectively, demonstrating that both B and P interact with the d orbital of metals through electron transfer. B donates electrons to the neighboring metallic atoms, while P receives electrons from the neighboring metallic atoms. This electron transportation between metallic elements and metalloids was also observed in previous reports [40, 52].

The OER electrocatalytic properties of the as-prepared samples were investigated in 1.0 M KOH aqueous electrolyte. The LSV curves measured between 1.2–1.7 V vs. RHE are shown in Fig. 3(a). As there is always an oxidation peak on the increasing-potential LSV curves of Ni-contained samples [53], the LSV curves of the Ni-contained samples in this work were measured reversely, i.e. from 1.7 to 1.2 V vs. RHE. To achieve an anodic current density of 10 mA/cm^2, FeCoNiPB requires a much smaller overpotential of 235 mV than FeCoPB (285 mV), FeNiPB

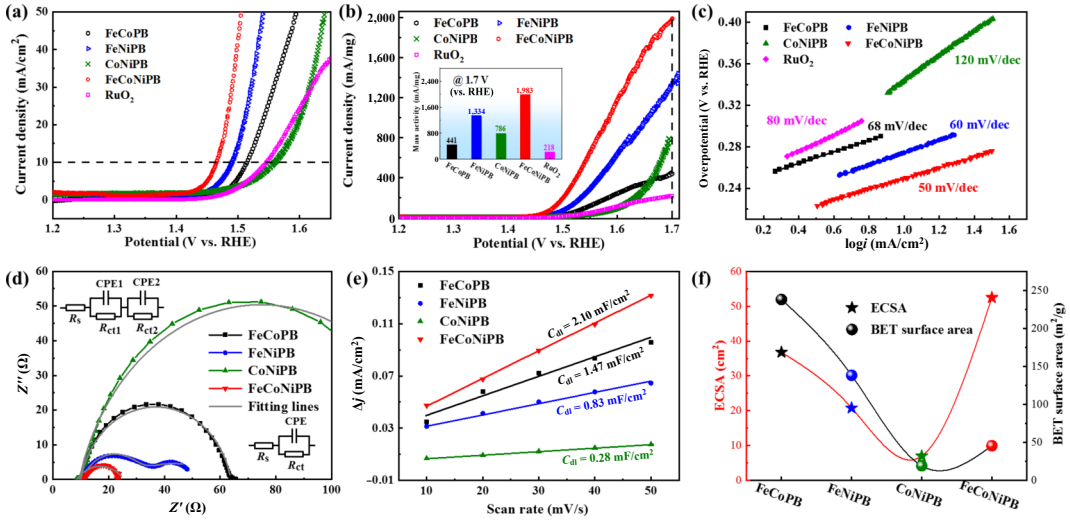

Figure 3 (a) LSV polarization curves (IR-corrected), (b) mass activity, and (c) corresponding Tafel plots of FeCoPB, FeNiPB, CoNiPB, FeCoNiPB, and RuO_2 for the OER in 1.0 M KOH. (d) Nyquist plots measured in 1.0 M KOH at an overpotential of 300 mV. Insets are the equivalent circuits for FeNiPB (upper left) and other three samples (bottom right). (e) Plots of capacitive current as a function of scan rates for electrocatalysts. (f) Comparison of the ECSA and BET surface areas of the FeCoPB, FeNiPB, CoNiPB, and FeCoNiPB samples.

(261 mV), CoNiPB (330 mV), and commercial RuO_2 (316 mV) catalysts. Notably, even at a higher current density of 100 mA/cm², FeCoNiPB remains a low overpotential of 306 mV, which is superior to most of the electrocatalysts that have been reported. The mass activity of the catalysts was obtained from the LSV curves, as shown in Fig. 3(b). The FeCoNiPB catalyst produces a much higher activity of 1,983 mA/mg under 1.7 V (vs. RHE) than FeCoPB (441 mA/mg), FeNiPB (1334 mA/mg), CoNiPB (786 mA/mg), and RuO_2 (218 mA/mg). This result further confirms the highly improved OER catalytic performance of FeCoNiPB sample.

To compare the OER reaction kinetics of the as-prepared samples and commercial RuO_2, the Tafel slopes were derived from LSV curves and are shown in Fig. 3(c). The Tafel slope of FeCoNiPB is 53 mV/dec, which is lower than those of FeCoPB (68 mV/dec), FeNiPB (60 mV/dec), CoNiPB (120 mV/dec), and RuO_2 (80 mV/dec). This result indicates the fastest OER reaction kinetics of FeCoNiPB catalyst. The charge transfer resistance on the surface of the samples was analyzed by EIS measurements. As shown in Fig. 3(d), the Nyquist plots of the four samples are fitted by equivalent circuits. The additional constant phase angle element CPE2 and charge transfer resistance R_{CT2} for FeNiPB sample represent the capacity and charge-transfer resistance caused by the surface product film layer [54], and both R_{ct1} and R_{ct2} contribute to the overall charge-transfer resistance of FeNiPB sample. The charge-transfer resistance of FeCoNiPB sample is only 16.9 Ω, which is much smaller than that of FeNiPB (47.6 Ω), FeCoPB (53.72 Ω), and CoNiPB (130.4 Ω), further evidencing the best electrocatalytic kinetics of FeCoNiPB [55].

The electrocatalytic activity is usually regarded to correlate with the ECSA, which is linearly proportional to the electrochemical C_{dl}. The C_{dl} value of the samples was measured by capacitance measurement via cyclic voltammograms (CVs) in the double-layer region with scan rates ranging from 10 to 50 mV/s [56], as shown in Fig. S11 in the ESM. The Δj values obtained from different scan rates for the as-prepared samples are shown in Fig. 3(e). Based on the fitting lines, the C_{dl} value of FeCoNiPB is 2.10 mF/cm², which is much higher than those of FeCoPB (1.47 mF/cm²), FeNiPB (0.83 mF/cm²), and CoNiPB (0.28 mF/cm²). Correspondingly, the ECSA of FeCoNiPB, FeCoPB, FeNiPB, and CoNiPB are calculated to be 52.5, 36.8, 20.8, and 7.0 cm², respectively. The ECSA and BET surface areas of the FeCoPB, FeNiPB, CoNiPB, and FeCoNiPB catalysts are summarized in Fig. 3(f). The FeCoNiPB catalyst exhibits a low specific surface area but the largest ECSA, revealing its high intrinsic activity. These results demonstrate the presence of more electrochemical active sites on the surface of FeCoNiPB catalyst. The OER Faradaic efficiency of the as-prepared FeCoNiPB sample was measured using the rotating ring-disk electrode (RRDE) technique in N_2-saturated 1.0 M KOH solution [57, 58], as shown in Fig. S12 in the ESM. The Faradaic efficiency of 96.3% further confirms the high catalytic efficiency of the as-prepared FeCoNiPB sample.

To compare with the representative non-precious OER electrocatalysts that have been reported recently, plots of the Tafel slope versus overpotential at a current density of 10 mA/cm² in 1.0 M KOH electrolyte are shown in Fig. 4(a). Details of the

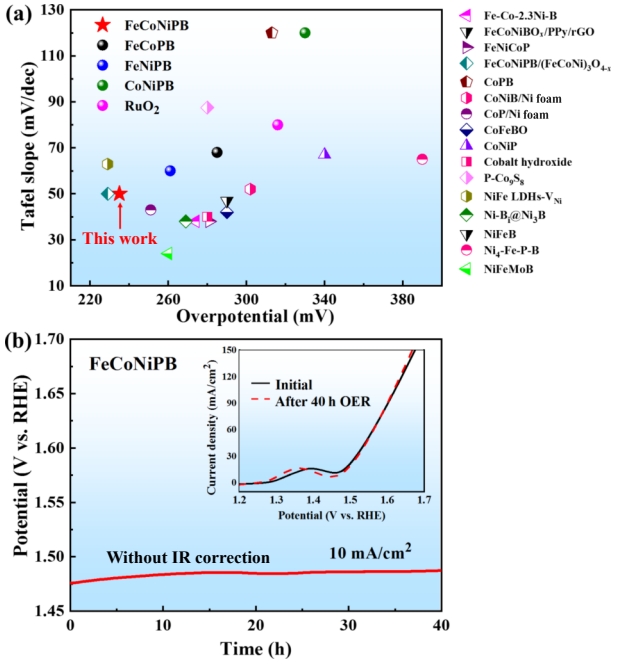

Figure 4 (a) Comparison of the overpotential (at a current density of 10 mA/cm²) and Tafel slope for representative nonprecious metal OER catalysts in 1.0 M KOH electrolytes. (b) Chronopotentiometric curve at a potential required to afford 10 mA/cm² in 1.0 M KOH at room temperature of FeCoNiPB catalyst. Inset shows the polarization curves (IR-corrected) of FeCoNiPB catalyst for initial OER catalysis and after continuous 40 h OER catalysis.

electrochemical properties, including constituents, morphology, phases, and substrates, are listed in Table S3 in the ESM. Obviously, the FeCoNiPB in this work has higher catalytic activity for the OER in alkaline media than most of the reported transition metal-based electrocatalysts. The overpotentials of NiFe layered double hydroxides (LDHs)-V_{Ni} and FeCoNiPB/$(FeCoNi)_3O_{4-x}$ are smaller than that of the FeCoNiPB under the same testing conditions [59]. However, the preparation of the NiFe LDHs-V_{Ni} synthesis requires high temperature and a strong base electrolyte, and FeCoNiPB/$(FeCoNi)_3O_{4-x}$ needs strong acids to dealloy, both of which make the preparation process more complicated. As a result, the FeCoNiPB catalyst synthesized by a facile reduction process in this work has superiority when considering the preparation cost and the catalytic activity simultaneously.

Another critical criterion to assess an electrocatalyst for practical electrochemical applications is durability. The electrocatalytic stability of FeCoNiPB catalyst was evaluated by the chronopotentiometry method at a current density of 10 mA/cm^2, as shown in Fig. 4(b). It exhibits an outstanding durability with only a negligible potential amplification of 11 mV after 40 h OER, showing a drift rate of 0.275 mV/h. As shown in the inset, the LSV polarization curves of the FeCoNiPB catalyst for the initial OER and after 40 h of continuous OER almost overlap. This shows that the catalyst is both highly efficient and stable, and can be a competitive candidate for OER catalysts with excellent comprehensive performance.

To uncover the origin of the outstanding stability, we analyzed the morphology and microstructure of the FeCoNiPB catalyst after 40 h of OER. As shown in the TEM images in Fig. 5(a), nanosheets structure is formed after long-term OER. The SAED pattern of the nanosheets structure only shows a large halo, revealing the overall amorphous state of the sample (inset of Fig. 5(a)). However, as shown in the HRTEM image in Fig. 5(b), the edge of the sheet-like structure exhibits a periodic lattice structure with a thickness of several nanometers, while the inner structure still maintains amorphous. The lattice spacing is approximately 2.30 Å, which can be assigned to crystalline CoOOH(111) [5]. It is well accepted that Ni, Fe, and Co-based alloys and oxides tend to chemically etch into Ni, Fe, and Co-oxyhydroxides, such as NiOOH, FeOOH, and CoOOH, in alkaline electrolyte during water electrolysis [5, 40, 42, 60], which are active sites for OER to attract hydroxyl groups owing to its hydrophilicity. Moreover, the HAADF and EDS analysis of the FeCoNiPB catalyst after long-term OER reveals a homogeneous distribution of the constituents, as shown in Fig. 5(c). However, the mapping of the P element evolves indiscernibly, and the signal of B elements cannot be detected at all, indicating a decrease in B and P elements on the surface. Based on the TEM and EDS analysis, it is confirmed that FeCoNiPB nanoparticles have self-reconstructed into amorphous sheets with a thin (FeCoNi)OOH crystalline layer on the edge after long-term OER. The ternary metals in the amorphous matrix lead to the formation of oxyhydroxides, and the sluggish diffusion

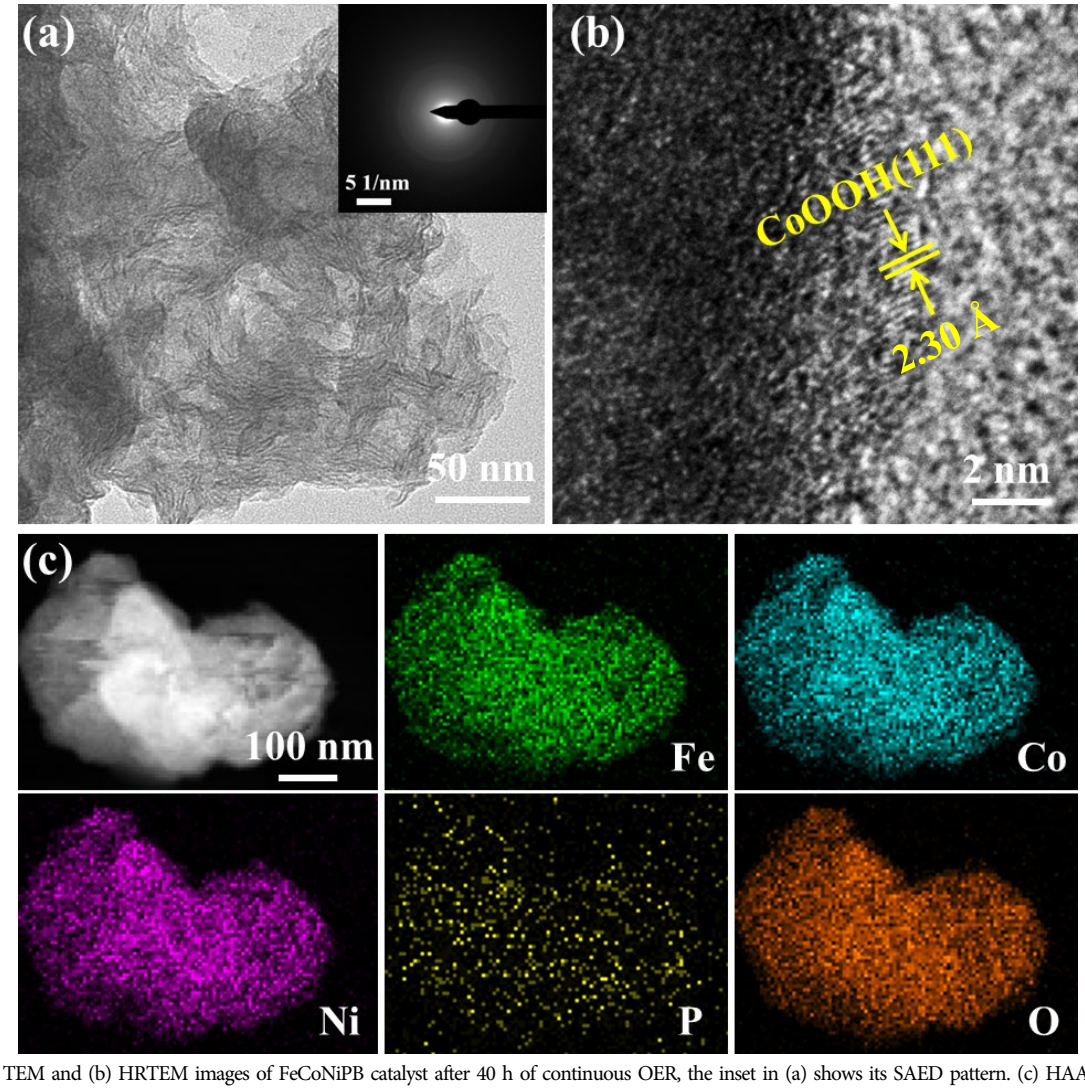

Figure 5 (a) TEM and (b) HRTEM images of FeCoNiPB catalyst after 40 h of continuous OER, the inset in (a) shows its SAED pattern. (c) HAADF image and elemental mappings of FeCoNiPB catalyst after 40 h continuous OER.

caused by the high-entropy effect may prevent further oxidation of the amorphous core. The morphological transformation of the FeCoNiPB from nanoparticles to sheets can be confirmed by the SEM analyses shown in Fig. S13 in the ESM. With chronopotentiometric testing for only 1 h, the sample almost completely changes to sheets morphology, indicating that the self-reconstruction occurs at the early stage. Thus, the amorphous sheets with metallic conductivity can provide fast electron transportation, while the formed (FeCoNi)OOH crystalline layer maintains the structure of the catalyst during long-term OER. Therefore, the unique self-reconstruction structure formed during the OER significantly contributes to both efficient activity and long-term stability.

To explore the variation in the chemical states of the FeCoNiPB catalyst after being subjected to potentiostatic durability tests in an alkaline medium, XPS characterizations were performed and are shown in Fig. 6. The zero-valent metals disappear completely, indicating that they are oxidized into higher valence states, such as Ni^{3+}, Fe^{3+}, and Co^{3+}. This is consistent with the formation of (FeCoNi)OOH on the surface obtained from the TEM analyses. Moreover, the binding energies of the oxidized states of Fe $2p_{3/2}$ and Ni $2p_{3/2}$ in the post-OER FeCoNiPB sample are similar to the as-prepared samples, where 711.5 eV is deconvoluted to Fe^{3+} and 856.9 eV is for Ni^{3+}. However, the oxidized Co in the as-prepared FeCoNiPB sample exhibits only one valence state of Co^{2+} and it completely transforms to Co^{3+} after the OER. The O 1s spectrum in Fig. 6(d) demonstrates that the degree of oxidation (74.8%) increases compared with that of the as-prepared sample, which is consistent with the formation of (FeCoNi)OOH crystallites on the surface. As shown in Figs. 6(e) and 6(f), the peaks of B 1s and P 2p are invisible, which is consistent with the EDS results in Fig. 5(c). The substantial decreases in the atomic percentages of P and B in the catalyst after the OER indicate that the metalloid elements on the surface will be severely corroded in the alkaline electrolyte during the OER [40]. For OER, it was reported that B in the electrolyte plays not only positive role by accelerating the PCET step, but also a negative role to adsorb active sites [61, 62]. Thus, the overall effect of the dissolved B in the electrolyte remains uncovered as it is difficult to quantify its positive or negative contribution.

4 Conclusion

In summary, the FeCoNiPB non-noble metal-based amorphous high-entropy oxides with superior electrocatalytic activity and stability for the OER have been prepared through an economically feasible and convenient chemical reduction method. The FeCoNiPB oxides show low overpotentials of 235 and 306 mV to drive the current densities of 10 and 100 mA/cm^2, respectively, while maintaining a reliable performance over 40 h. The unique amorphous high-entropy structure and synergistic effect of ternary metals (Fe, Co, and Ni) and metalloids (P, B) improve the OER performance. Moreover, it is found that the formation of a thin (FeCoNi)OOH crystalline layer during the long-term OER retains the high-efficiency and stability of the catalyst. This work provides a prospective design strategy for non-noble metal-based amorphous high-entropy oxides electrocatalysts for the OER process.

Acknowledgments

This work was supported by the National Natural Science Foundation of China (No. 51631003) and the Natural Science Foundation of Jiangsu Province (No. BK20191269).

Electronic Supplementary Material: Supplementary material (the

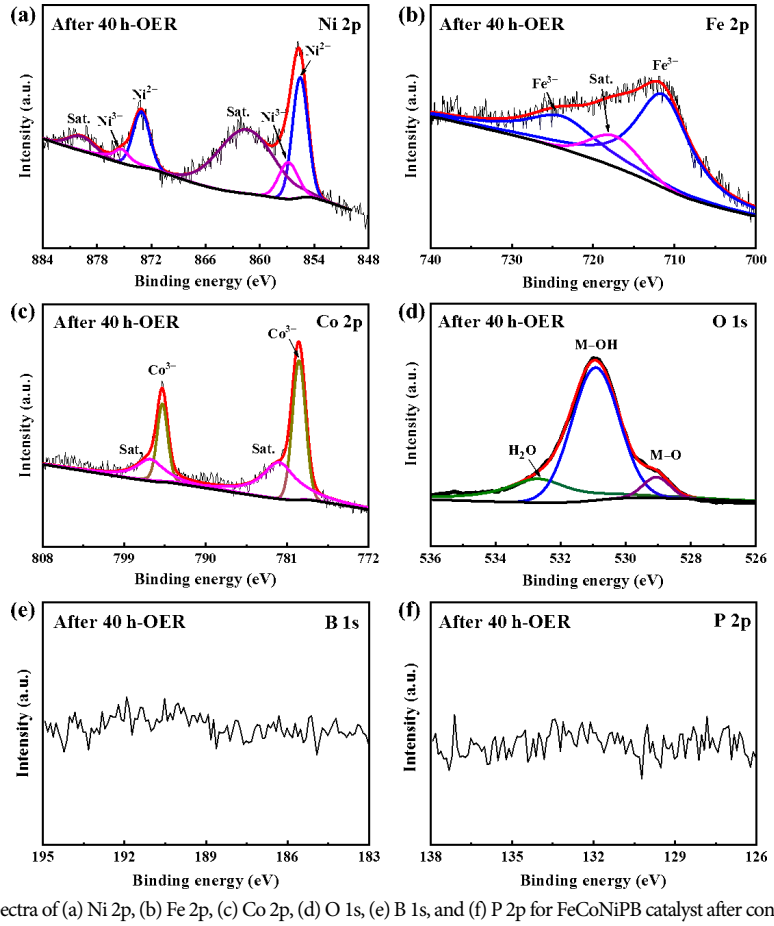

Figure 6 High-resolution XPS spectra of (a) Ni 2p, (b) Fe 2p, (c) Co 2p, (d) O 1s, (e) B 1s, and (f) P 2p for FeCoNiPB catalyst after continuous 40 h OER.

calibration of reference electrode, characterization of FeCoPB, FeNiPB, and CoNiPB samples (SEM images, TEM images, EDS mappings, and XPS spectra), CV curves, Faradaic efficiency testing, tables of the TEM-EDS composition and XPS binding energies for the samples, and tables of OER performance comparison) is available in the online version of this article at https://doi.org/10.1007/s12274-022-4179-8.

References

[1] Ghoniem, A. F. Needs, resources and climate change: Clean and efficient conversion technologies. *Prog. Energy Combust. Sci.* **2011**, *37*, 15–51.

[2] Zeng, M.; Li, Y. G. Recent advances in heterogeneous electrocatalysts for the hydrogen evolution reaction. *J. Mater. Chem. A* **2015**, *3*, 14942–14962.

[3] Santos, D. M. F.; Sequeira, C. A. C.; Figueiredo, J. L. Hydrogen production by alkaline water electrolysis. *Quim. Nova* **2013**, *36*, 1176–1193.

[4] Qi, J.; Zhang, W.; Cao, R. Solar-to-hydrogen energy conversion based on water splitting. *Adv. Energy Mater.* **2018**, *8*, 1701620.

[5] Liu, G.; He, D. Y.; Yao, R.; Zhao, Y.; Li, J. P. Amorphous NiFeB nanoparticles realizing highly active and stable oxygen evolving reaction for water splitting. *Nano Res.* **2018**, *11*, 1664–1675.

[6] Wang, Z. L.; Xu, D.; Xu, J. J.; Zhang, X. B. Oxygen electrocatalysts in metal-air batteries: From aqueous to nonaqueous electrolytes. *Chem. Soc. Rev.* **2014**, *43*, 7746–7786.

[7] Fu, J.; Cano, Z. P.; Park, M. G.; Yu, A. P.; Fowler, M.; Chen, Z. W. Electrically rechargeable zinc-air batteries: Progress, challenges, and perspectives. *Adv. Mater.* **2017**, *29*, 1604685.

[8] Jiao, Y.; Zheng, Y.; Jaroniec, M.; Qiao, S. Z. Design of electrocatalysts for oxygen- and hydrogen-involving energy conversion reactions. *Chem. Soc. Rev.* **2015**, *44*, 2060–2086.

[9] Glasscott, M. W.; Pendergast, A. D.; Goines, S.; Bishop, A. R.; Hoang, A. T.; Renault, C.; Dick, J. E. Electrosynthesis of high-entropy metallic glass nanoparticles for designer, multi-functional electrocatalysis. *Nat. Commun.* **2019**, *10*, 2650.

[10] Jia, Z.; Yang, T.; Sun, L. G.; Zhao, Y. L.; Li, W. P.; Luan, J. H.; Lyu, F. C.; Zhang, L. C.; Kruzic, J. J.; Kai, J. J. et al. A novel multinary intermetallic as an active electrocatalyst for hydrogen evolution. *Adv. Mater.* **2020**, *32*, 2000385.

[11] Ju, S.; Feng, J. Q.; Zou, P.; Xu, W.; Wang, S. J.; Gao, W. B.; Qiu, H. J.; Huo, J. T.; Wang, J. Q. A robust self-stabilized electrode based on Al-based metallic glasses for a highly efficient hydrogen evolution reaction. *J. Mater. Chem. A* **2020**, *8*, 3246–3251.

[12] Batchelor, T. A. A.; Pedersen, J. K.; Winther, S. H.; Castelli, I. E.; Jacobsen, K. W.; Rossmeisl, J. High-entropy alloys as a discovery platform for electrocatalysis. *Joule* **2019**, *3*, 834–845.

[13] Löffler, T.; Savan, A.; Garzón-Manjón, A.; Meischein, M.; Scheu, C.; Ludwig, A.; Schuhmann, W. Toward a paradigm shift in electrocatalysis using complex solid solution nanoparticles. *ACS Energy Lett.* **2019**, *4*, 1206–1214.

[14] Zhao, X. H.; Xue, Z. M.; Chen, W. J.; Wang, Y. Q.; Mu, T. C. Eutectic synthesis of high-entropy metal phosphides for electrocatalytic water splitting. *ChemSusChem* **2020**, *13*, 2038–2042.

[15] Gludovatz, B.; Hohenwarter, A.; Catoor, D.; Chang, E. H.; George, E. P.; Ritchie, R. O. A fracture-resistant high-entropy alloy for cryogenic applications. *Science* **2014**, *345*, 1153–1158.

[16] Jin, Z. Y.; Lv, J.; Jia, H. L.; Liu, W. H.; Li, H. L.; Chen, Z. H.; Lin, X.; Xie, G. Q.; Liu, X. J.; Sun, S. H. et al. Nanoporous Al-Ni-Co-Ir-Mo high-entropy alloy for record-high water splitting activity in acidic environments. *Small* **2019**, *15*, 1904180.

[17] Qiu, H. J.; Fang, G.; Gao, J. J.; Wen, Y. R.; Lv, J.; Li, H. L.; Xie, G. Q.; Liu, X. J.; Sun, S. H. Noble metal-free nanoporous high-entropy alloys as highly efficient electrocatalysts for oxygen evolution reaction. *ACS Mater. Lett.* **2019**, *1*, 526–533.

[18] Sharma, L.; Katiyar, N. K.; Parui, A.; Das, R.; Kumar, R.; Tiwary, C. S.; Singh, A. K.; Halder, A.; Biswas, K. Low-cost high entropy alloy (HEA) for high-efficiency oxygen evolution reaction (OER). *Nano Res.*, in press, https://doi.org/10.1007/s12274-021-3802-4.

[19] Li, H. D.; Han, Y.; Zhao, H.; Qi, W. J.; Zhang, D.; Yu, Y. D.; Cai, W. W.; Li, S. X.; Lai, J. P.; Huang, B. L. et al. Fast site-to-site electron transfer of high-entropy alloy nanocatalyst driving redox electrocatalysis. *Nat. Commun.* **2020**, *11*, 5437.

[20] Zhang, Y.; Lu, T.; Ye, Y. K.; Dai, W. J.; Zhu, Y. A.; Pan, Y. Stabilizing oxygen vacancy in entropy-engineered $CoFe_2O_4$-type catalysts for Co-prosperity of efficiency and stability in an oxygen evolution reaction. *ACS Appl. Mater. Interfaces* **2020**, *12*, 32548–32555.

[21] Hu, Y. C.; Wang, Y. Z.; Su, R.; Cao, C. R.; Li, F.; Sun, C. W.; Yang, Y.; Guan, P. F.; Ding, D. W.; Wang, Z. L. et al. A highly efficient and self-stabilizing metallic-glass catalyst for electrochemical hydrogen generation. *Adv. Mater.* **2016**, *28*, 10293–10297.

[22] Miao, F.; Wang, Q. Q.; Zhang, L. C.; Shen, B. L. Magnetically separable Z-scheme FeSiB metallic glass/g-C_3N_4 heterojunction photocatalyst with high degradation efficiency at universal pH conditions. *Appl. Surf. Sci.* **2021**, *540*, 148401.

[23] Tan, Y. W.; Zhu, F.; Wang, H.; Tian, Y.; Hirata, A.; Fujita, T.; Chen, M. W. Noble-metal-free metallic glass as a highly active and stable bifunctional electrocatalyst for water splitting. *Adv. Mater. Interfaces* **2017**, *4*, 1601086.

[24] Li, R.; Liu, X. J.; Wu, R. Y.; Wang, J.; Li, Z. B.; Chan, K. C.; Wang, H.; Wu, Y.; Lu, Z. P. Flexible honeycombed nanoporous/glassy hybrid for efficient electrocatalytic hydrogen generation. *Adv. Mater.* **2019**, *31*, 1904989.

[25] Wang, Z. J.; Li, M. X.; Yu, J. H.; Ge, X. B.; Liu, Y. H.; Wang, W. H. Low-iridium-content IrNiTa metallic glass films as intrinsically active catalysts for hydrogen evolution reaction. *Adv. Mater.* **2020**, *32*, 1906384.

[26] Jia, Z.; Duan, X. G.; Qin, P.; Zhang, W. C.; Wang, W. M.; Yang, C.; Sun, H. Q.; Wang, S. B.; Zhang, L. C. Disordered atomic packing structure of metallic glass: Toward ultrafast hydroxyl radicals production rate and strong electron transfer ability in catalytic performance. *Adv. Funct. Mater.* **2017**, *27*, 1702258.

[27] Zhang, L. C.; Jia, Z.; Lyu, F. C.; Liang, S. X.; Lu, J. A review of catalytic performance of metallic glasses in wastewater treatment: Recent progress and prospects. *Prog. Mater. Sci.* **2019**, *105*, 100576.

[28] Li, B.; Chen, S. M.; Tian, J.; Gong, M.; Xu, H. X.; Song, L. Amorphous nickel-iron oxides/carbon nanohybrids for an efficient and durable oxygen evolution reaction. *Nano Res.* **2017**, *10*, 3629–3637.

[29] Johny, J.; Li, Y.; Kamp, M.; Prymak, O.; Liang, S. X.; Krekeler, T.; Ritter, M.; Kienle, L.; Rehbock, C.; Barcikowski, S. et al. Laser-generated high entropy metallic glass nanoparticles as bifunctional electrocatalysts. *Nano Res.*, in press, https://doi.org/10.1007/s12274-021-3804-2.

[30] Hu, F.; Zhu, S. L.; Chen, S. M.; Li, Y.; Ma, L.; Wu, T. P.; Zhang, Y.; Wang, C. M.; Liu, C. C.; Yang, X. J. et al. Amorphous metallic NiFeP: A conductive bulk material achieving high activity for oxygen evolution reaction in both alkaline and acidic media. *Adv. Mater.* **2017**, *29*, 1606570.

[31] Zhang, F. B.; Wu, J. L.; Jiang, W.; Hu, Q. Z.; Zhang, B. New and efficient electrocatalyst for hydrogen production from water splitting: Inexpensive, robust metallic glassy ribbons based on iron and cobalt. *ACS Appl. Mater. Interfaces* **2017**, *9*, 31340–31344.

[32] Li, S. M.; Yang, X. H.; Yang, S. Y.; Gao, Q. Z.; Zhang, S. S.; Yu, X. Y.; Fang, Y. P.; Yang, S. H.; Cai, X. An amorphous trimetallic (Ni-Co-Fe) hydroxide-sheathed 3D bifunctional electrode for superior oxygen evolution and high-performance cable-type flexible zinc-air batteries. *J. Mater. Chem. A* **2020**, *8*, 5601–5611.

[33] Lee, S.; Banjac, K.; Lingenfelder, M.; Hu, X. L. Oxygen isotope labeling experiments reveal different reaction sites for the oxygen evolution reaction on nickel and nickel iron oxides. *Angew. Chem., Int. Ed.* **2019**, *58*, 10295–10299.

[34] Kibsgaard, J.; Chorkendorff, I. Considerations for the scaling-up of water splitting catalysts. *Nat. Energy* **2019**, *4*, 430–433.

[35] Zeng, Y. Q.; Yu, J. S.; Tian, Y.; Hirata, A.; Fujita, T.; Zhang, X. H.; Nishiyama, N.; Kato, H.; Jiang, J. Q.; Inoue, A. et al. Improving glass forming ability of off-eutectic metallic glass formers by manipulating primary crystallization reactions. *Acta Mater.* **2020**,

200, 710–719.

[36] Wu, Z. X.; Nie, D. Z.; Song, M.; Jiao, T. T.; Fu, G. T.; Liu, X. E. Facile synthesis of Co-Fe-B-P nanochains as an efficient bifunctional electrocatalyst for overall water-splitting. *Nanoscale* **2019**, *11*, 7506–7512.

[37] Zhang, B.; Zheng, X. L.; Voznyy, O.; Comin, R.; Bajdich, M.; García-Melchor, M.; Han, L. L.; Xu, J. X.; Liu, M.; Zheng, L. R. et al. Homogeneously dispersed multimetal oxygen-evolving catalysts. *Science* **2016**, *352*, 333–337.

[38] Wu, Y. H.; Lian, J. Q.; Wang, Y. X.; Sun, J. J.; He, Z.; Gu, Z. J. Potentiostatic electrodeposition of self-supported Ni-S electrocatalyst supported on Ni foam for efficient hydrogen evolution. *Mater. Des.* **2021**, *198*, 109316.

[39] Zhang, X.; Zhang, X.; Xu, H. M.; Wu, Z. S.; Wang, H. L.; Liang, Y. Y. Iron-doped cobalt monophosphide nanosheet/carbon nanotube hybrids as active and stable electrocatalysts for water splitting. *Adv. Funct. Mater.* **2017**, *27*, 1606635.

[40] Tang, W. K.; Liu, X. F.; Li, Y.; Pu, Y. H.; Lu, Y.; Song, Z. M.; Wang, Q.; Yu, R. H.; Shui, J. L. Boosting electrocatalytic water splitting via metal-metalloid combined modulation in quaternary Ni-Fe-P-B amorphous compound. *Nano Res.* **2020**, *13*, 447–454.

[41] Popczun, E. J.; McKone, J. R.; Read, C. G.; Biacchi, A. J.; Wiltrout, A. M.; Lewis, N. S.; Schaak, R. E. Nanostructured nickel phosphide as an electrocatalyst for the hydrogen evolution reaction. *J. Am. Chem. Soc.* **2013**, *135*, 9267–9270.

[42] Chunduri, A.; Gupta, S.; Bapat, O.; Bhide, A.; Fernandes, R.; Patel, M. K.; Bambole, V.; Miotello, A.; Patel, N. A unique amorphous cobalt-phosphide-boride bifunctional electrocatalyst for enhanced alkaline water-splitting. *Appl. Catal. B:Environ.* **2019**, *259*, 118051.

[43] Zhang, P. L.; Wang, M.; Yang, Y.; Yao, T. Y.; Han, H. X.; Sun, L. C. Electroless plated Ni-B_x films as highly active electrocatalysts for hydrogen production from water over a wide pH range. *Nano Energy* **2016**, *19*, 98–107.

[44] Löffler, T.; Waag, F.; Gökce, B.; Ludwig, A.; Barcikowski, S.; Schuhmann, W. Comparing the activity of complex solid solution electrocatalysts using inflection points of voltammetric activity curves as activity descriptors. *ACS Catal.* **2021**, *11*, 1014–1023.

[45] Waag, F.; Li, Y.; Ziefuß, A. R.; Bertin, E.; Kamp, M.; Duppel, V.; Marzun, G.; Kienle, L.; Barcikowski, S.; Gökce, B. Kinetically-controlled laser-synthesis of colloidal high-entropy alloy nanoparticles. *RSC Adv.* **2019**, *9*, 18547–18558.

[46] Jiang, S. D.; Tian, K. H.; Li, X. L.; Duan, C. Q.; Wang, D.; Wang, Z. Y.; Sun, H. Y.; Zheng, R. G.; Liu, Y. G. Amorphous high-entropy non-precious metal oxides with surface reconstruction toward highly efficient and durable catalyst for oxygen evolution reaction. *J. Colloid Interface Sci.* **2022**, *606*, 635–644.

[47] Elgrishi, N.; Rountree, K. J.; McCarthy, B. D.; Rountree, E. S.; Eisenhart, T. T.; Dempsey, J. L. A practical beginner' s guide to cyclic voltammetry. *J. Chem. Educ.* **2018**, *95*, 197–206.

[48] Jia, Z.; Nomoto, K.; Wang, Q.; Kong, C.; Sun, L. G.; Zhang, L. C.; Liang, S. X.; Lu, J.; Kruzic, J. J. A self-supported high-entropy metallic glass with a nanosponge architecture for efficient hydrogen evolution under alkaline and acidic conditions. *Adv. Funct. Mater.* **2021**, *31*, 2101586.

[49] Nsanzimana, J. M. V.; Dangol, R.; Reddu, V.; Duo, S.; Peng, Y. C.; Dinh, K. N.; Huang, Z. F.; Yan, Q. Y.; Wang, X. Facile synthesis of amorphous ternary metal borides-reduced graphene oxide hybrid with superior oxygen evolution activity. *ACS Appl. Mater. Interfaces* **2019**, *11*, 846–855.

[50] Wang, X. X.; She, G. W.; Mu, L. X.; Shi, W. S. Amorphous Co-Mo-P-O bifunctional electrocatalyst via facile electrodeposition for overall water splitting. *ACS Sustainable Chem. Eng.* **2020**, *8*, 2835–2842.

[51] Jiang, N.; You, B.; Sheng, M. L.; Sun, Y. J. Electrodeposited cobalt-phosphorous-derived films as competent bifunctional catalysts for overall water splitting. *Angew. Chem., Int. Ed.* **2015**, *54*, 6251–6254.

[52] Xu, M.; Han, L.; Han, Y. J.; Yu, Y.; Zhai, J. F.; Dong, S. J. Porous CoP concave polyhedron electrocatalysts synthesized from metal-organic frameworks with enhanced electrochemical properties for hydrogen evolution. *J. Mater. Chem. A* **2015**, *3*, 21471–21477.

[53] Zhang, N.; Feng, X. B.; Rao, D. W.; Deng, X.; Cai, L. J.; Qiu, B. C.; Long, R.; Xiong, Y. J.; Lu, Y.; Chai, Y. Lattice oxygen activation enabled by high-valence metal sites for enhanced water oxidation. *Nat. Commun.* **2020**, *11*, 4066.

[54] Guo, L. S.; Yu, B. X.; Zhou, P.; Zhang, T.; Wang, F. H. Fabrication of low-cost Ni-P composite coating on Mg alloys with a significant improvement of corrosion resistance: Critical role of mitigating the galvanic contact between the substrate and the coating. *Corros. Sci.* **2021**, *183*, 109329.

[55] Jia, Z.; Wang, Q.; Sun, L. G.; Wang, Q.; Zhang, L. C.; Wu, G.; Luan, J. H.; Jiao, Z. B.; Wang, A. D.; Liang, S. X. et al. Attractive *in situ* self-reconstructed hierarchical gradient structure of metallic glass for high efficiency and remarkable stability in catalytic performance. *Adv. Funct. Mater.* **2019**, *29*, 1807857.

[56] Chen, R.; Wang, H. Y.; Miao, J. W.; Yang, H. B.; Liu, B. A flexible high-performance oxygen evolution electrode with three-dimensional $NiCo_2O_4$ core–shell nanowires. *Nano Energy* **2015**, *11*, 333–340.

[57] Zhao, S. L.; Wang, Y.; Dong, J. C.; He, C. T.; Yin, H. J.; An, P. F.; Zhao, K.; Zhang, X. F.; Gao, C.; Zhang, L. J. et al. Ultrathin metal-organic framework nanosheets for electrocatalytic oxygen evolution. *Nat. Energy* **2016**, *1*, 16184.

[58] Suntivich, J.; May, K. J.; Gasteiger, H. A.; Goodenough, J. B.; Shao-Horn, Y. A perovskite oxide optimized for oxygen evolution catalysis from molecular orbital principles. *Science* **2011**, *334*, 1383–1385.

[59] Wang, Y. Y.; Qiao, M.; Li, Y. F.; Wang, S. Y. Tuning surface electronic configuration of NiFe LDHs nanosheets by introducing cation vacancies (Fe or Ni) as highly efficient electrocatalysts for oxygen evolution reaction. *Small* **2018**, *14*, 1800136.

[60] Xu, Z. J. Transition metal oxides for water oxidation: All about oxyhydroxides? *Sci. China Mater.* **2020**, *63*, 3–7.

[61] Bediako, D. K.; Lassalle-Kaiser, B.; Surendranath, Y.; Yano, J.; Yachandra, V. K.; Nocera, D. G. Structure-activity correlations in a nickel-borate oxygen evolution catalyst. *J. Am. Chem. Soc.* **2012**, *134*, 6801–6809.

[62] Bediako, D. K.; Surendranath, Y.; Nocera, D. G. Mechanistic studies of the oxygen evolution reaction mediated by a nickel-borate thin film electrocatalyst. *J. Am. Chem. Soc.* **2013**, *135*, 3662–3674.